RESEARCH ARTICLE

# Time-resolved stereo PIV measurements of shock–boundary layer interaction on a supercritical airfoil

**Axel Hartmann · Michael Klaas · Wolfgang Schröder**

**Abstract** Time-resolved stereo particle-image velocimetry (TR-SPIV) and unsteady pressure measurements are used to analyze the unsteady flow over a supercritical DRA-2303 airfoil in transonic flow. The dynamic shock wave–boundary layer interaction is one of the most essential features of this unsteady flow causing a distinct oscillation of the flow field. Results from wind-tunnel experiments with a variation of the freestream Mach number at Reynolds numbers ranging from 2.55 to $2.79 \times 10^6$ are analyzed regarding the origin and nature of the unsteady shock–boundary layer interaction. Therefore, the TR-SPIV results are analyzed for three buffet flows. One flow exhibits a sinusoidal streamwise oscillation of the shock wave only due to an acoustic feedback loop formed by the shock wave and the trailing-edge noise. The other two buffet flows have been intentionally influenced by an artificial acoustic source installed downstream of the test section to investigate the behavior of the interaction to upstream-propagating disturbances generated by a defined source of noise. The results show that such upstream-propagating disturbances could be identified to be responsible for the upstream displacement of the shock wave and that the feedback loop is formed by a pulsating separation of the boundary layer dependent on the shock position and the sound pressure level at the shock position. Thereby, the pulsation of the separation could be determined to be a reaction to the shock motion and not vice versa.

A. Hartmann (✉) · M. Klaas · W. Schröder
Institute of Aerodynamics, RWTH Aachen University,
Aachen, Germany
e-mail: a.hartmann@aia.rwth-aachen.de
URL: www.aia.rwth-aachen.de

## 1 Introduction

The flow field of modern supercritical airfoils in transonic flow is characterized by a local supersonic region on the upper surface terminated by a shock wave. A highly complex and unsteady flow pattern may develop in the direct vicinity of the surface, e.g., a shock-induced separation of the turbulent boundary layer may occur. Moreover, the time-dependent interaction of the shock wave with the boundary layer in the transonic flight regime may lead to an oscillation of the shock wave generating pressure fluctuations acting on the wing structure as time-dependent load distribution. Since the flow downstream of the shock is subsonic, a feedback loop of disturbances propagating both upstream and downstream may be formed amplifying the shock oscillation and the pressure fluctuations acting on the structure. This phenomenon is commonly known as transonic Buffet, and accordingly Buffeting when the interaction with the structure is considered. Hence, wings of modern transport aircraft with optimized light-weight design may exhibit a distinctive structural response to unsteady loads.

To understand this phenomenon, series of wind-tunnel tests have been conducted with the supercritical laminar-type airfoil DRA-2303. The experiments have been performed in a transonic intermittent vacuum-storage wind tunnel at freestream Mach numbers between $M_\infty = 0.64$ and 0.78 at Reynolds numbers ranging from 2.55 to $2.79 \times 10^6$ and angles of attack between $\alpha = 0$ and 4°. The airfoil flow exhibits an increased degree of unsteadiness at a Mach number range between $M_\infty = 0.72$ and 0.73 and angles of attack between $\alpha = 2$ and 4° due to a dynamic interaction between the shock wave and the turbulent boundary layer, eventually causing a trailing-edge separation. To get insight into the origin of the shock wave

movement, the influence of an artificial acoustic source installed downstream of the airfoil model on the shock wave–boundary layer interaction is investigated. This acoustic source generates upstream-propagating disturbances that interact with the shock wave comparable to upstream-propagating disturbances generated by the trailing-edge noise of the airfoil. In the literature, upstream traveling sound waves generated at the trailing edge of the airfoil have been identified as the main buffet mechanism (Lee 2001). However, this model is based on experimental studies on a pitching symmetric airfoil with the shock motion being delayed by the time so-called Kutta waves, which are associated with the lift variation, take to propagate upstream to the shock location as well as a numerical study with an impulse disturbance located at the trailing edge (Tijdeman 1977; Lee et al. 1994).

Flow field information is obtained using three-component time-resolved stereo particle-image velocimetry (TR-SPIV) to capture any three-dimensional characteristics in the flow field. Furthermore, a blurring of the particle images in the vicinity of the shock wave as reported by Elsinga et al.( 2005) is avoided using this approach, since a viewing angle that is oblique to the sharp shock front only results in a displacement of the particles caused by the change of the refractive index. For a maximum local Mach number of $M = 1.2$, the resulting density variation is $\rho_2/\rho_1 = 2.67$. Consequently, the variation of the refractive index can be calculated using the Gladstone–Dale relation to be $n_2/n_1 = 1.000107769$ indicating that the influence of the optical disturbances can be neglected for the chosen angle of view of 36°.

Additional to the PIV measurements, steady and unsteady pressure measurements as well as high-speed Schlieren imaging have been applied.

The paper possesses the following structure. First, the experimental setup is introduced followed by the results of the experiments. The results are discussed for three transonic flows with distinct flow field characteristics. Then, the results for the same flows but influenced by an acoustic source installed downstream of the test section are discussed. Finally, the main findings are summarized.

## 2 Experimental setup

### 2.1 Wind tunnel

The experimental investigation has been conducted in the Trisonic Wind Tunnel of the RWTH Aachen University. This facility is an intermittently working vacuum-storage tunnel producing flows at Mach numbers ranging from 0.4 to 3.0. Depending on the Mach number, the entire test run lasts about 10 s with 2–3 s of stable flow with a turbulence

intensity below 1% (Guntermann 1992). For transonic flows at freestream Mach numbers below one, the tunnel is equipped with a 0.4 m × 0.4 m 2-D adaptive test section consisting of parallel side walls and flexible upper and bottom walls to simulate unconfined flow conditions (Romberg 1990). The wall contours are calculated by the one-step method solving the Cauchy integral based on the time-averaged pressure distribution measured along the center line of the flexible walls (Amecke 1985). The total pressure and temperature of the wind tunnel are determined by the ambient conditions. Therefore, the unit Reynolds number depends on the Mach number, and ambient temperature ranging from 1.2 to 1.4 × 10⁷ m⁻¹ in the present experiments. The relative humidity of the flow is kept below 4% using a drier at total temperatures of about 293 K to exclude any influence on the shock wave position (Binion 1988). The dried air is stored in the settling balloon of the tunnel prior to each test run.

The acoustic environment in the wind tunnel is of major interest for the experimental simulation of dynamic fluid interaction processes. For this reason, the adaptive test section is equipped with 26 dynamic pressure transducers distributed along the centerline of the upper and lower wall. The standard configuration of the wind tunnel does not show any distinct resonance frequencies, and the RMS value of pressure fluctuations is below 1%. To create an artificial acoustic source for the second part of the experimental investigation, the parallel upper and lower walls indicated in Figs. 1 and 4, which guide the flow through the freestream chamber of the tunnel downstream of the test section, are removed. This leads to a free-shear-layer-flow at certain disturbances that are amplified by the volume of the freestream chamber and that propagate upstream into the test section. In this configuration, the power spectra of the pressure transducers in the test section evidence a peak around 248 Hz for the Mach number range under investigation.
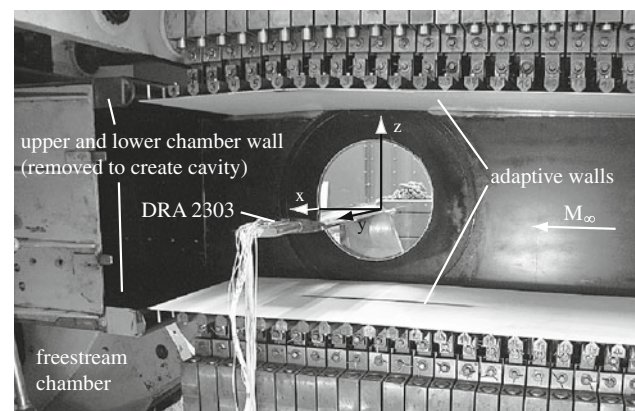


**Fig. 1** Adaptive test section with removed sidewall and DRA 2303 airfoil model installed

The fluctuation level of the pressure values decays significantly with the distance of the transducers from the freestream chamber indicating that although the disturbances propagate upstream, they do not influence the freestream flow conditions entering the test section.

## 2.2 Airfoil model

The rigid airfoil model is the supercritical laminar-type profile DRA-2303, which has been under investigation in the Euroshock project (Stanewsky et al. 1997). The airfoil has a relative thickness to chord ratio of 14% and a chord length of $c = 200$ mm. The laminar-turbulent transition of the boundary layer is fixed at 5% chord using a 117-μm zigzag-shaped transition strip. The model is equipped with 11 Kulite XCQ-080 subminiature pressure transducers in the area of the shock–boundary layer interaction ranging from $x/c = 0.45$ to 0.7 on the upper surface. The distance between the pressure taps is 0.025 $x/c$. Each transducer is installed in closest proximity to the corresponding pressure orifice to minimize the damping and phase shift of the measured pressure signal against the actual signal on the airfoil surface (Fig. 2).

Figure 3 shows the dynamic response of the sensor installation plotted against the reduced frequency $\omega^* = 2\pi fc/u_\infty$ in the Mach number range of $0.8 \leq M \leq 1.4$ relevant for the flow conditions under consideration. The response function was calculated using the theory developed by Tijdeman (1965) for the propagation of small harmonic pressure perturbations through tube-transducer systems. The calculations show that the response function has a very small influence on pressure fluctuations in the reduced frequency range of $\omega^* < 3$ of the flow field oscillation which is investigated in this study. This corresponds to a true value of less than 790 Hz at $M = 1$. Nevertheless, the phase shift $\Phi_u/\Phi_i$ and the gain $p_u/p_i$, with $u$ denoting the original value and $i$ the measured value, are considered for the data evaluation using a first-order approximation for the transfer function developed by Tijdeman (1965). In Fig. 2, the approximation of the transfer function is compared with the original function for
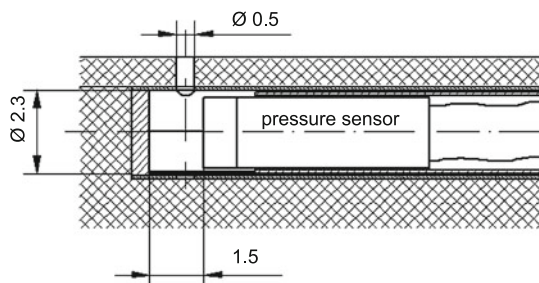


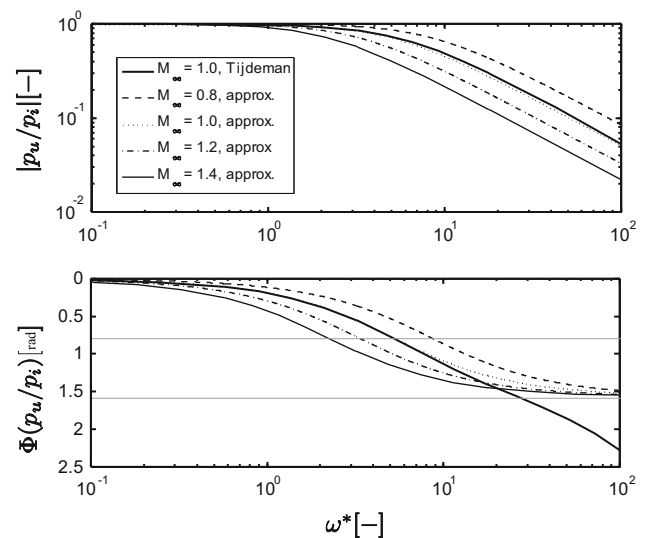Fig. 2 Pressure transducer installation, dimensions given in mm



Fig. 3 Modulus and phase of sensor installation dynamic response as a function of the reduced frequency $\omega^*$ for $0.8 \leq M \leq 1.4$

$M = 1$ showing the validity of the approximation for the relevant frequency range of $\omega^* < 3$. The approximate ion allows to calculate the original pressure value $p_u$ at the pressure orifice

$$p_u = p_i + Tp_i' \qquad (1)$$

with $T$ being the time constant which is determined for each Mach number using the transfer function by Tijdeman.

The pressure transducer signals are recorded by a data acquisition (DAQ) system consisting of five data acquisition boards Imtec T-112 with simultaneous analog-to-digital conversion of 40 channels, 12 bit resolution, and up to 1.25 MHz sampling rate per channel. In the present experiments, a sampling rate of $f_{DAQ}^s = 20$ kHz was selected. The signals are conditioned with 4-pole Butterworth low-pass filtering with 10 kHz corner frequency and hundredfold amplification with a bandwidth of 100 kHz by Endevco 136 DC-amplifiers.

For steady pressure measurements, the model comprises 25 pressure taps on the upper surface and 19 pressure taps on the lower surface. The distance between the pressure taps is $0.05x/c$ except for $x/c = 0.45$–0.7 on the upper surface with a distance of is $0.025x/c$.

## 2.3 TR-SPIV setup

In addition to pressure measurements, three-component time-resolved stereo particle-image velocimetry (TR-SPIV) with the laser light sheet positioned parallel to the incoming flow has been employed to analyze the flow field from $x/c \approx 0.4$–0.9 on the test section center line. Droplets of Di-Ethyl-Hexyl-Sebacat (DEHS, CAS-No. 122-62-3) were used as seeding with a mean diameter of 0.6 μm as per

datasheet of the Topas GmbH ATM 242 atomizer. To achieve a homogenous seeding distribution, the seeding was added to the flow in the dry air reservoir of the wind tunnel prior to each test run. The particle response time $\tau_p$ can be calculated to be approximately 1.98 µs using the approach mentioned, e.g., by Melling (1986) corresponding to a frequency response of $f_s = 505$ kHz.

The flow was illuminated using a Quantronix Darwin Duo 40-M double-pulsed Nd: YLF laser with a wavelength of 527 nm. The repetition rate was set to 1,500 Hz resulting in an energy of approximately 15 mJ per pulse. The thickness of the laser light sheet was about 1 mm. The optical access for the laser beam was provided through an aperture in the freestream chamber of the wind tunnel downstream of the test section as denoted in Fig. 4. Using the frame-straddling technique mentioned by Raffel et al. (2007), the laser pulse separation in the experiments was 3.4 µs leading to a mean particle displacement of approximately 1 mm corresponding to approximately 10 pixels in the acquired flow images. The particle images were recorded by two Photon Fastcam SA-3 CMOS cameras in Scheimpflug condition with a viewing angle of 36°. Both cameras record the forward scatter of the particles as shown in Fig. 4. The cameras are equipped with a $1,024 \times 1,024$ pixel-sized sensor capable to achieve a frame rate of 2,000 Hz at full resolution.
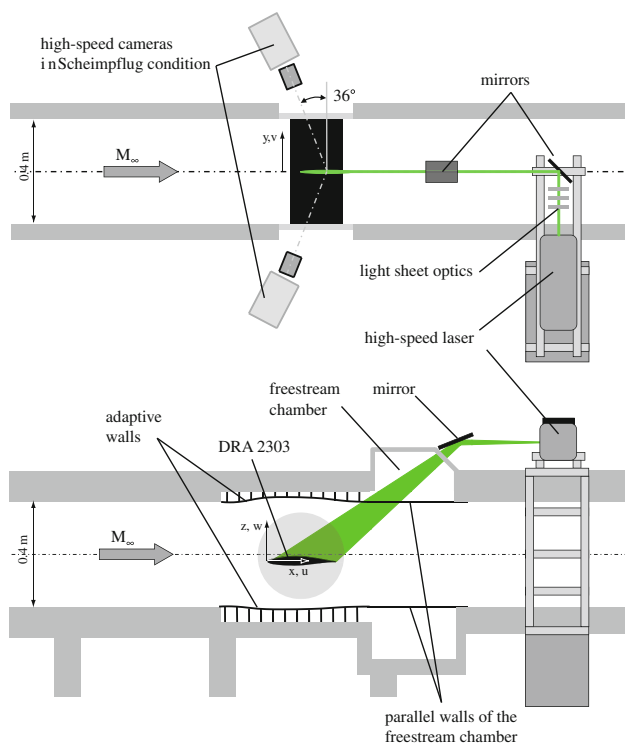


**Fig. 4** Plan view (*top*) and side view (*bottom*) of the TR-SPIV setup

The sensor was cropped to $1,024 \times 512$ pixels to achieve an increased recording rate of 3,000 Hz leading to a sampling rate of $f_s^{PIV} = 1,500$ Hz. This frequency is 6 times higher than the highest frequency of the shock oscillation measured with the Kulite pressure transducers, thus fulfilling the Nyquist criterion. Furthermore, the spectra achieved from the TR-SPIV measurements perfectly agree with the pressure spectra obtained with 20 kHz such that we define the SPIV measurements as time resolved regarding the shock wave oscillation. Two 100-mm Tokina 1:2.8 macro lenses were mounted to the cameras. The optical settings result in a particle diameter of approximately 3 pixels in the recorded images. The resulting field of view covers an area, which reaches from $x/c = 0.38$ to 0.85 and from the wing surface to $z/c = 0.2$. Figure 3 depicts an overview of the test setup.

In each test run, a dataset of 2,726 image pairs was acquired. The images were analyzed using the ILA Vid-PIV software using multi-pass adaptive cross-correlation schemes with window shift and deformation. Prior to the evaluation, the images of each camera were dewarped using the information of a calibration target placed into the light sheet plane. This perspective mapping of the images is done by a Tsai model (Tsai 1986) that is based on the pin-hole model of perspective projection. Due to a misalignment of the calibration target with respect to the laser light sheet, a certain error cannot be excluded in the reconstruction of the *x*- and *y*-velocity components from the two component vector fields. This error can be corrected by determining the local misalignment using the approach of Willert (1997) by calculating a so-called disparity map. The disparity map is used to improve the mapping functions so that the final disparity is minimized. The dewarped and disparity corrected images are evaluated using adaptive cross-correlation with window shifting and deformation schemes. The final window size was $32 \times 32$ pixels with an overlap factor of 50%. This leads to a vector spacing of 1.50 mm with 98% of valid vectors. To post-process the data, a window velocity filter, which filters velocity vectors that are outside an adjustable range, and a normalized local median filter as described in Westerweel and Scarano (2005) have been used to identify and remove outliers. Then, the stereoscopic reconstruction is applied to calculate the third velocity component. Again, the reconstruction is based on the parameters of the Tsai model. To remove spurious vectors, the third velocity component is locally filtered after the reconstruction leading to an amount of 95% of non-interpolated vectors.

For the synchronization of the TR-SPIV and the time-resolved pressure measurements, the exposure signal of the camera of each frame was recorded with the DAQ system

used for the pressure transducer signals leading to a maximum time discrepancy of 25 μs due to the different recording rates of 3 and 20 kHz, respectively.

Exposure tests with the Nd:YLF high-speed laser with 15 mJ pulse energy showed a significant local heating of the airfoil surface in the area illuminated by the laser light sheet due to absorption of the araldite gel coat layer. To avoid any deterioration of the surface quality and structural stiffness, a 10-mm-wide and 0.2-mm-thick 3-M aluminum tape is integrated into the wing surface. The tape, which serves as a heat sink by diffusing the absorbed laser energy, is flush-mounted by applying it onto the surface during the model manufacturing process to avoid any surface distortion.

## 2.4 Schlieren imaging

Due to the limited spatial extension of the PIV measurement plane, high-speed Schlieren imaging (HSI) has been applied to qualitatively visualize the integral density gradient distribution of the entire flow field on the upper surface of the airfoil. It has been applied synchronously with unsteady pressure measurements mentioned above. The Schlieren technique employs a standard Z-type Schlieren setup (Tropea et al. 2007). The Schlieren images were recorded by a Photron SA-3 high-speed camera described above. The recording rate was set to $f_s^{HSI} = 3{,}000$ Hz.

## 3 Results

In the following, the results of the wind-tunnel measurements are analyzed. The airfoil aerodynamics has been investigated for angles of attack ranging from $\alpha = 0$ to 4°, freestream Mach numbers between $M_\infty = 0.64$ and 0.78, and Reynolds numbers $Re_\infty$ related to the chord length $c$ in the range of 2.55–2.79 $\times$ 10$^6$. Three transonic flows are discussed in detail. All flows have been investigated twice, once with the tunnel in standard configuration, i.e., the aforementioned parallel walls are part of the freestream chamber, and once without these walls such that an acoustic source downstream of the test section is generated. This is denoted by the subscript 'as' throughout the paper. The flow conditions being analyzed in the article are summarized in Table 1.

### 3.1 Time-averaged flow analysis

The unsteady aerodynamic flow field of the airfoil is dominated by flow characteristics, which are accessible to time-averaged flow measurement tools. The main feature of the transonic airfoil flow is a compression shock

**Table 1** Investigated flow conditions

| Case | $Re_\infty$ | $\alpha$ (°) | $M_\infty$ | $\alpha_{as}$ (°) | $M_{\infty,as}$ | Occurence of buffet |
|------|------------|------|------|------|------|------|
| I | $2.55 \times 10^6$ | 1 | 0.67 | | | |
| II | $2.63 \times 10^6$ | 3 | 0.72 | | | × |
| III | $2.79 \times 10^6$ | 3 | 0.76 | | | |
| I$_{as}$ | $2.55 \times 10^6$ | | | 1 | 0.67 | |
| II$_{as}$ | $2.63 \times 10^6$ | | | 3 | 0.72 | × |
| III$_{as}$ | $2.79 \times 10^6$ | | | 3 | 0.76 | × |
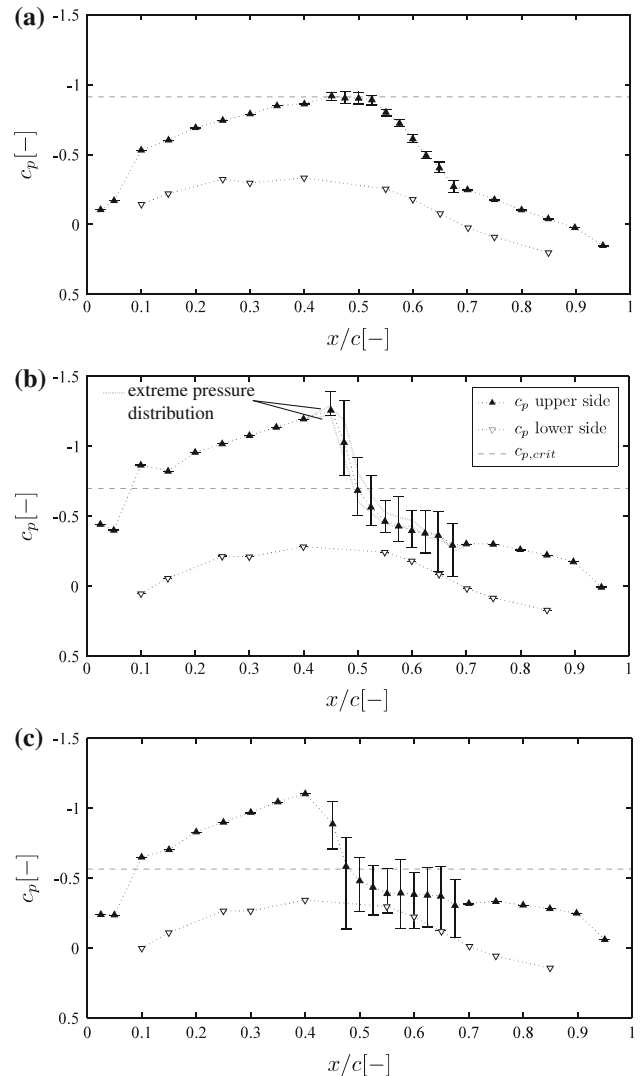
**Fig. 5** Time-averaged pressure distribution at case I **a**, case II **b,** and case III **c**

terminating the supersonic pocket in the flow field. Figure 5 exemplarily displays the time-averaged pressure distribution for $M_\infty = 0.67$ at an angle of attack of $\alpha = 1°$ (case I) and $M_\infty = 0.72$ and 0.76 at an angle of attack of $\alpha = 3°$ (case II, III), respectively. The flow field at case I is

just critical since the pressure level just drops to the critical value $c_{p,crit}$, which is included in the plots, followed by a smooth pressure rise. The unsteadiness of the flow is shown by the length of the *error bars* denoting the local maximum and minimum measured independently by each of the 11 unsteady pressure transducers raging from $x/c = 0.45$–$0.7$ during the experiment. For the critical flow at $M_\infty = 0.67$, the error bars do not show any significant unsteadiness. The supersonic flow area grows at increasing freestream Mach number and angle of attack leading to a stronger shock. At case II, the shock is indicated by the steep pressure rise at $x/c = 0.45$–$0.5$ with the highest amount of unsteadiness located at the shock position. The extreme pressure distributions for the shock location at its most upstream and its most downstream position indicate a small oscillation of the shock at this flow case. The relatively slow pressure rise downstream of the shock wave also indicates a separation of the flow at an alternating chordwise position.

At case III, the steep pressure rise caused by the shock wave appears to be smoothed. This is caused by the limited resolution of the pressure taps upstream of $x/c = 0.45$. The strong shock wave at these flow conditions is followed by a steady flow separation downstream of the shock system indicated by the pressure plateau in Fig. 5c. This marks the change from a mild to a severe interaction with the boundary layer, which is consistent with the commonly known Mach number effect on the transonic flow field described by Seddon (1960), Green (1970), Adamson and Messiter (1980), Délery (1985), Délery and Marvin (1986).

In the following, the time-averaged pressure distribution for the above flow cases is discussed, but this time with the acoustic source installed downstream of the test section.

The time-averaged pressure distribution of the critical flow at case $I_{as}$ in Fig. 6a does not show any significant changes. The level of unsteadiness has increased due to the disturbances generated in the freestream chamber. At case $II_{as}$ and $III_{as}$, the steep pressure rise is smoothed by the time averaging and the fluctuation level has increased significantly. This evidences a large-scale motion of the shock wave in the streamwise direction followed by a separation. The extreme pressure distributions also show this large-scale motion of the shock at cases $II_{as}$ and $III_{as}$. The relatively slow pressure rise downstream of the shock indicates that the detachment location of the flow is time dependent. This converts into a pressure plateau at case III in Fig. 6c substantiating the interpretation of the steady separation caused by the stronger shock wave. The fact that the remaining mean pressure distribution does not change remarkable compared to the cases without the source installed shows that the acoustic source primarily influences the shock wave and not the entire boundary conditions.
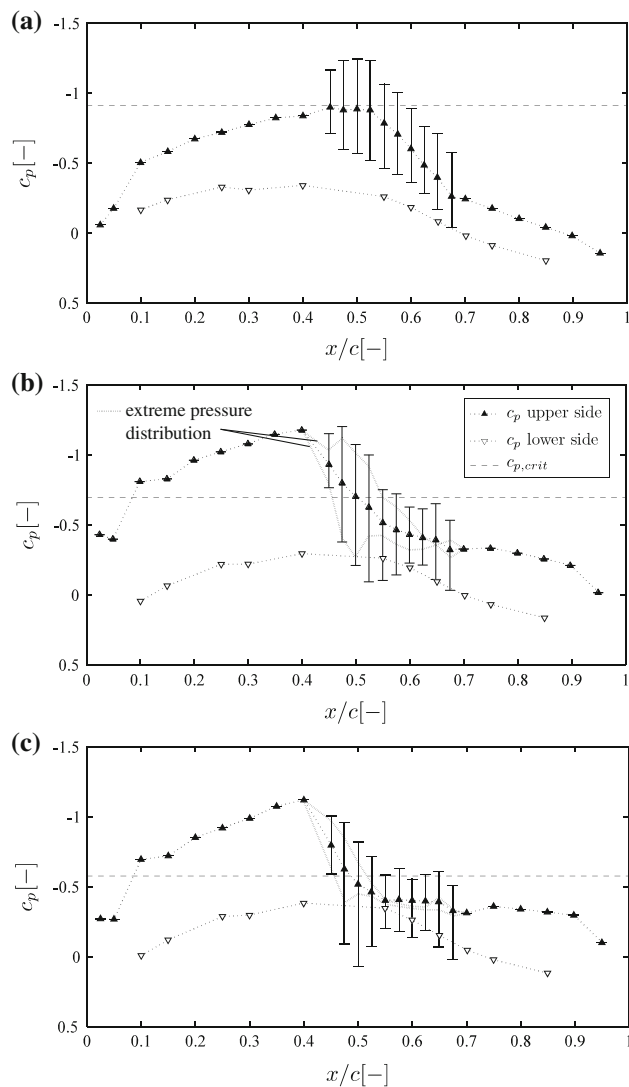


**Fig. 6** Time-averaged pressure distribution at case $I_{as}$ **a**, case $II_{as}$ **b**, and case $III_{as}$ **c**

### 3.2 Time-resolved flow analysis

#### 3.2.1 Pressure distribution

Periodic shock oscillations have been investigated in several experimental and numerical studies. Brunet et al. (2006) describe a "pulsation" of the separated area to be the origin of buffet oscillations on the OAT15A supercritical airfoil with a thickness to chord ratio of 12.5%. In his widely accepted shock buffet model, Lee (2001) describes the inviscid shock interaction with upstream-propagating sound waves, which are generated by the impingement of large-scale turbulent eddies on the sharp trailing edge forming a feedback loop with disturbances convected downstream. This is also defined as the main buffet mechanism (Deck 2005).

Following the analysis discussed in the literature, the temporal development of the present flow fields is investigated in greater detail. First, the undistorted flow cases are analyzed, and subsequently, the flow fields with the artificial acoustic source installed downstream of the test section with upstream-propagating disturbances are presented. The impact of the temporal development on specific flow patterns like, e.g., the oscillation of the shock wave has been already illustrated by the smoothing effects contained in the pressure distributions caused by flow unsteadiness (Fig. 6). The strongest surface pressure fluctuations can be found in the region of the shock position and downstream of the shock caused by the interaction with the boundary layer.
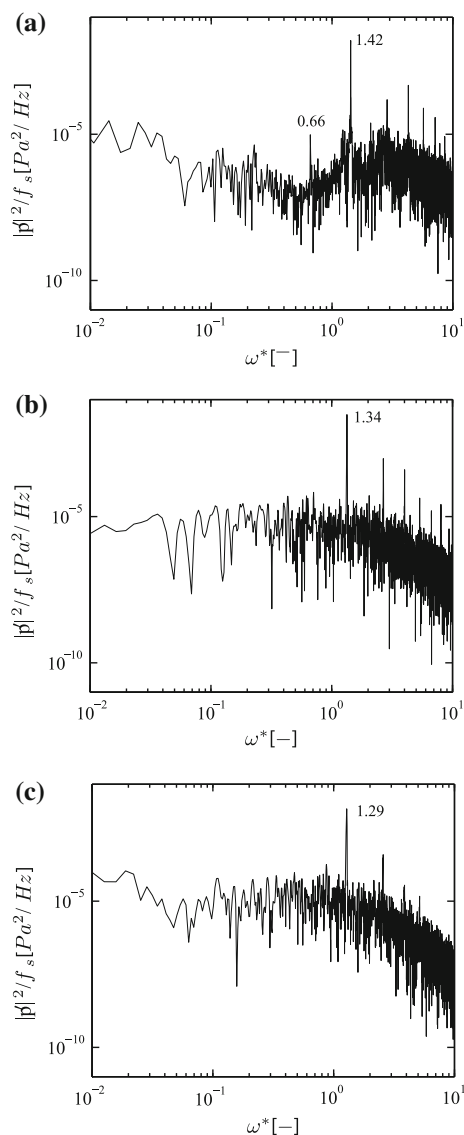
The power spectral density of the pressure fluctuations $p'$ sampled with $f_{DAQ}^s = 20$ kHz at $x/c = 0.5$ for the shock-free flow at case I in Fig. 7a shows that the flow field is steady without any distinct fluctuation frequencies. In Fig. 7b at case II, the fluctuation level is significantly higher and an increased fluctuation level around $\omega^* = 0.68$ (125.5 Hz) is contained in the spectra. A reduced buffet frequency of $\omega^* = 0.55$ was measured by Schewe et al. (2002) for the NLR-7301 airfoil. Hartmann et al. (2011) detected a buffet frequency of $\omega^* = 0.72$ on a BAC 3–11 swept wing configuration. Finke (1977) and Lee (2001) measured shock buffet frequencies of $\omega^* = 0.5$–$2.0$ for the NACA 63-012 profile and $\omega^* = 0.5$ for the BGK No. 1 airfoil with a relative thickness of 11.8%. Hence, the measured reduced buffet frequency of $\omega^* = 0.68$ at $M_\infty = 0.72$ on the DRA-2303 airfoil is in the range of other supercritical airfoils with a comparable thickness ratio and shock position. Furthermore, a reduced buffet frequency of $\omega^* \approx 0.65$ at $M_\infty = 0.702$ and $\alpha = 2.4°$ has been measured for the DRA-2303 airfoil in the Euroshock project (Stanewsky et al. 1997). The flow with the stronger shock wave at case III does not show such a distinct increase of the fluctuation level at a certain frequency band compared to case II, though a little bump in the spectra in Fig. 7c around $\omega^* = 0.68$ (131.5 Hz) occurs. This means that the small scale shock motion which is also present in this case is less periodic than in case II. The spectra in Fig. 6 are representative in quality for the entire upper surface. To show the effect of upstream-propagating disturbances on the shock displacement, we now turn to the discussion of the impact of the downstream located artificial acoustic source on the surface pressure distribution. The spectra of pressure signals for the shock-free flow at case $I_{as}$ contain distinct harmonic peaks in $\omega^* = 0.66$ and $1.42$ (113.7 and 245 Hz), illustrating the periodic nature of the flow (Fig. 8a). When the shock pattern occurs at case $II_{as}$, the frequency of $1.34$ (248.4 Hz) dominates the flow field (Fig. 8b). At case $III_{as}$, the fluctuations become
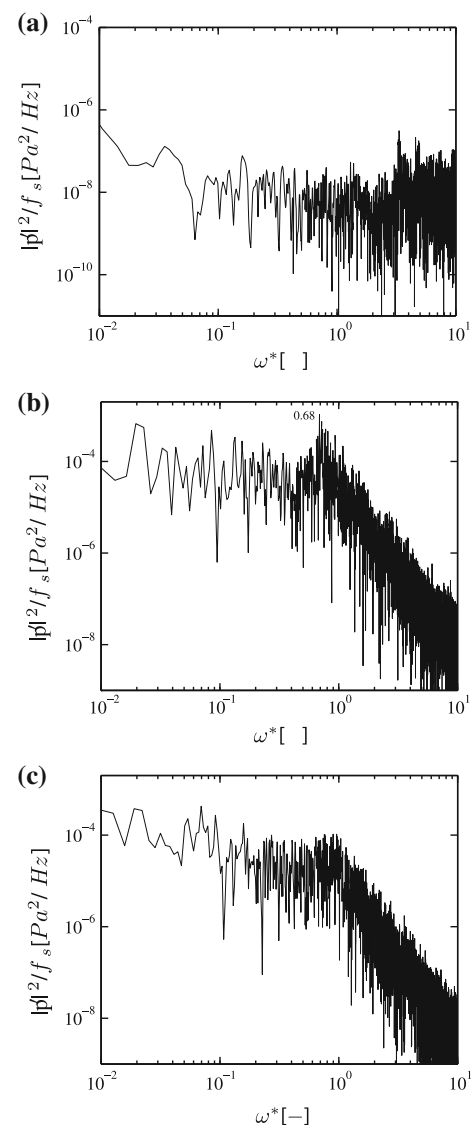


**Fig. 7** Power spectral analysis of the pressure signal at $x/c = 0.55$ at case I **a**, case II **b**, and case III **c**. Note the various scalings $f_{DAQ}^s = 20$ kHz

somewhat smaller at a frequency of $\omega^* = 1.29$ (249.9 Hz) (Fig. 8c). The normalized frequency of the oscillation slightly changes as a function of Mach number $M_\infty$, while the frequency of the disturbances generated by the freestream chamber remains almost alike at 248 Hz.
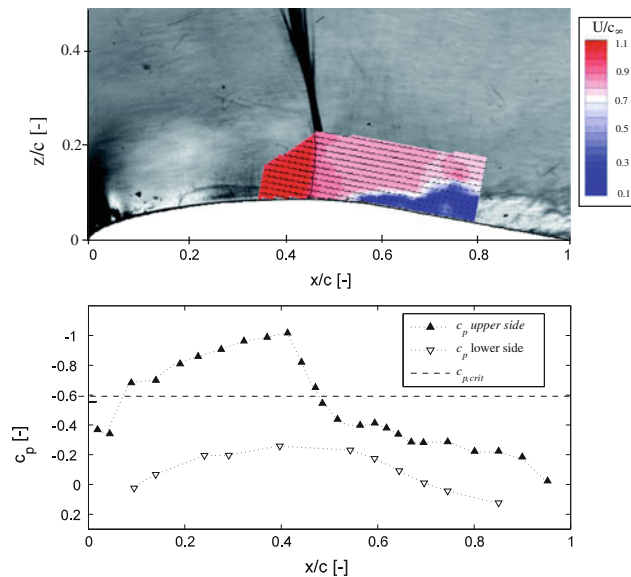
This shows that the frequency of the shock wave oscillation is dominated by these disturbances which force the natural shock-wave oscillation of the airfoil to lock into this resonance frequency. A comparable behavior has been predicted in a computational study by Raveh and Dowell (2009) in terms of a forced pitching oscillation of a NACA 0012 airfoil. In the present case, the disturbances excite the second mode of the natural buffet frequency of $\omega^* = 0.68$ since their frequency is about double this natural frequency

**(a)**



**(b)**



**(c)**



**Fig. 8** Power spectral analysis of the pressure signal at $x/c = 0.55$ case $I_{as}$ **a**, case $II_{as}$ **b**, and case $III_{as}$ **c**; $f^s_{DAQ} = 20$ kHz



**Fig. 9** Instantaneous velocity, density gradient, and pressure distribution at case $II_{as}$

such that the observed lock-in effect occurs. The power spectra of the shock-free flow at case $I_{as}$ also show a distinct peak at $\omega^* = 0.66$ associated with the undisturbed acoustic feedback loop of the airfoil. As soon as the shock wave occurs, solely the frequency of the downstream disturbances is present in the power spectra. That is, the sensitive shock wave directly locks into the frequency of the generated fluctuations, and the shock wave oscillation also governs the sound production at the trailing edge of the airfoil.

In the case of classical buffet, the shock is strong enough to cause a fully separated flow between the shock–boundary layer interaction and the trailing edge. The formation of the acoustic feedback loop can be observed at high Mach numbers and high angles of attack. In the disturbed DRA-

2303 buffet flow cases considered here, these disturbances lead to an oscillatory shock motion due to the interference between the noise of this artificial source and the noise generated by the trailing edge plus the shock wave. The various flow structures will be discussed in the following based on the velocity distributions.

### 3.2.2 Velocity distribution

To gain information on the velocity field, the TR-SPIV method is used to measure the unsteady flow around the DRA-2303 airfoil in the vicinity of the shock–boundary layer interaction zone. The vertical measurement plane is located along the center line of the adaptive test section in the streamwise direction. Figure 9 depicts a qualitative combination of an instantaneous velocity field measured by the TR-SPIV method and the respective pressure distribution and the density gradient in the flow field from Schlieren imaging at case $II_{as}$. The image evidences the location of the TR-SPIV measurement plane and illustrates the surrounding flow field. The three measurement techniques agree in terms of the shock-wave location and the extension of the shock-induced separation present in this flow case.

The airfoil flow field on the upper side under subcritical conditions is also determined by a separation of the boundary layer at the trailing edge. The separation occurs in the area of the positive pressure gradient. At increasing Mach numbers, the detachment line moves upstream and coincides with the shock position when the shock is strong enough to induce separation. Therefore, the flow development found for the DRA-2303 airfoil resembles the type

B3 flow in the phenomenological description given by Pearcey et al. (1968).

In the following, TR-SPIV results are presented together with the synchronous measured pressure distribution in the range of $x/c = 0.35$–0.85. Since the spanwise velocity component is very small compared to the main flow, it can be neglected and only the absolute velocity values based on the $x$- and $z$-components $U = \sqrt{u^2 + w^2}$ normalized by the freestream speed of sound $c_\infty$ are presented. The results are discussed for three flow conditions, which show a significant streamwise oscillation of the shock wave. That is, from Table 1, the undisturbed flow case II at $[\alpha, M_\infty] = [3°, 0.72]$ and the flow cases $II_{as}$ and $III_{as}$ influenced by the

additional acoustic source at $[\alpha_{as}, M_{\infty,as}] = [3°, 0.72]$ and $[3°, 0.76]$, respectively, are discussed.

*3.2.2.1 Case II* The image time series in Fig. 10 represents one time sequence for the undisturbed buffet case at $[\alpha, M_\infty] = [3°, 0.72]$. Note that only every second, time step is shown. The cycle starts at time step $t = \tilde{t}$ with the shock wave located at its most downstream position at $x/c = 0.49$. In the subsequent time steps, the shock wave moves upstream until it reaches its most upstream position $x/c = 0.46$ at $\tilde{t} + 4\Delta t$ before it moves back to $x/c = 0.49$ in the remaining time steps. Quasi-harmonic large-scale shock motions were first categorized by Tijdeman (1977).
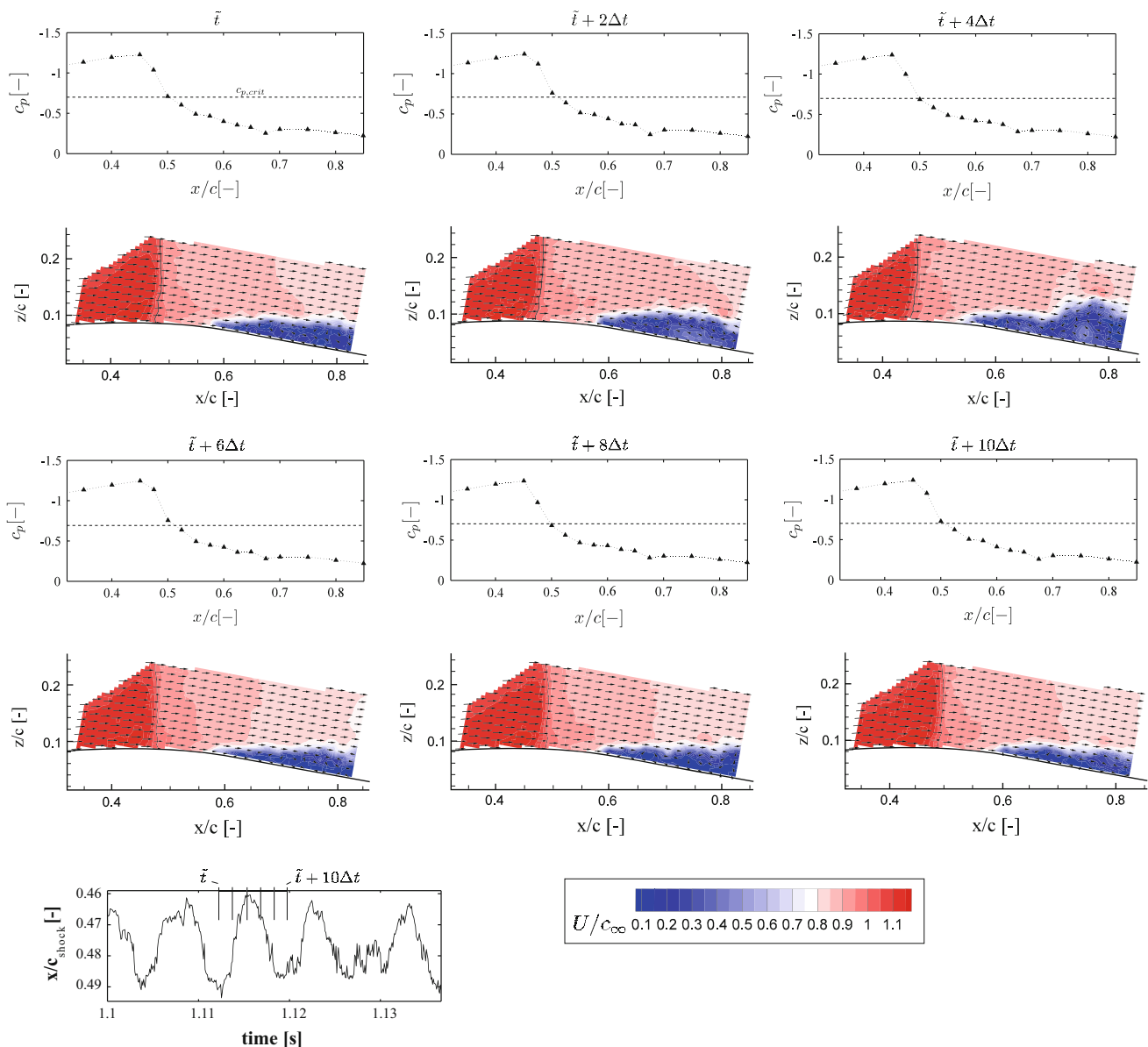


**Fig. 10** Time sequence of synchronously measured pressure distribution and velocity field at case II, time step $\Delta t = 0.67$ ms, the *black solid line* marks the $U/c_\infty = 1$ contour, every third vector plotted

The present purely sinusoidal motion with an amplitude of 4% chord can be classified as a Tijdeman type A motion.

The main buffet mechanism of the undisturbed case can be identified as an interaction of upstream propagation sound waves interacting with the shock wave as proposed by Lee (2001). The sound pressure level of the disturbances at the location of the shock wave varies with the extension of the boundary-layer separation, which is directly connected to the shock position. This strong correlation is shown in Fig. 11, where the shock position is plotted against the angle $\beta$ of the streamlines relative to the surface at $x/c = 0.7$ just outside of the separated flow region. At time step $\tilde{t} + 4\Delta t$, the extension of the separation at the trailing edge has increased compared to time step $\tilde{t}$. The various separation regions are also pictured by the Reynolds-stress distributions in Fig. 12. The larger separation means that the noise generated at the trailing edge has decreased since the velocity gradient near the trailing edge is less pronounced resulting in a different noise source. The noise generation area has widened, and the sound waves undergo a strong refraction in the free-shear layer yielding a weakened sound pressure level, which interacts with the shock wave. Since the thickening of the boundary layer propagates downstream at time steps $\tilde{t} + 2\Delta t$ and $\tilde{t} + 4\Delta t$ in Fig. 10, the thickening of the separation is regarded as a reaction to the shock wave motion and not vice versa. The above findings are underlined by the results of the disturbed buffet flows discussed in the following.

*3.2.2.2 Case II$_{as}$*  At time step $t = \tilde{t}$, Fig. 13 shows for case II$_{as}$ the shock wave close to its most downstream position at $x/c = 0.55$. Note that due to the doubled oscillation frequency, every single time step is shown. In the following at $t = \tilde{t} + 1\Delta t$ up to $\tilde{t} + 4\Delta t$, the supersonic
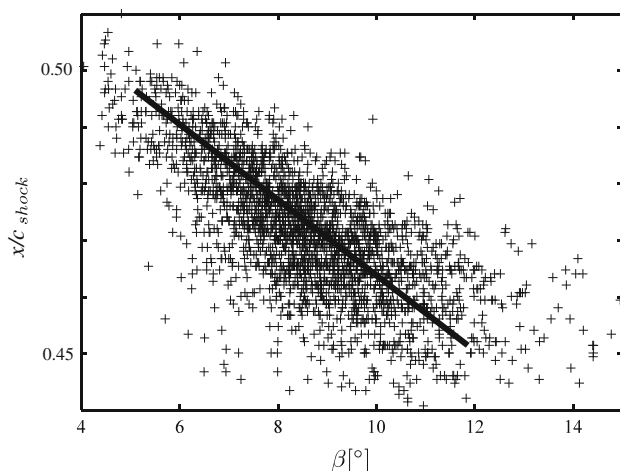


**Fig. 11** Shock position versus flow angle $\beta$ measured at $x/c = 0.7$ and $z/c = 0.15$ at case II
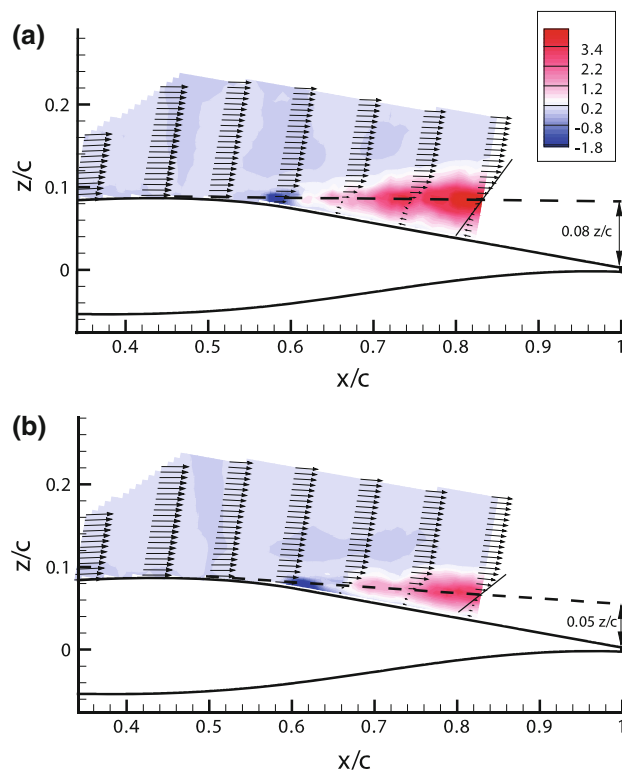


**Fig. 12** Reynolds-shear-stress distribution $(-\overline{u'w'}/U)$ and phase-averaged velocity profiles at case II and **a** the shock located most upstream at $x/c = 0.46$ and **b** most downstream at $x/c = 0.49$

region starts to shrink. This shrinkage is accompanied by an accelerating upstream motion of the shock wave. During this upstream shock motion, the local supersonic flow field loses its strength due to the characteristic pressure distribution of the airfoil resulting in a weakening of the shock wave. At time step $\tilde{t} + 4\Delta t$, the shock foot has reached its most upstream position at $x/c = 0.45$. In the next time step, the primary supersonic region has almost vanished, and according to the PIV images, the normal shock wave appears to turn into an oblique shock wave in $\tilde{t} + 5\Delta t$. Note that since the PIV measurement plane is limited to $x/c = 0.38$, the formation of the oblique shock is not well displayed. However, it can be derived from measurements at similar flow conditions and the maximum shock position located further downstream as well as from Schlieren images. The resulting deflection of the streamlines toward the airfoil surface results in an expansion downstream of the oblique shock wave so that the flow fulfills the boundary conditions at the wall. A second supersonic flow region that is closed by a weak shock wave is formed. The development of this second region marks the beginning of the new cycle. One time step later, the second region has grown significantly in terms of spatial extension as well as strength and the subsequent time step the flow field looks similar to that of the first time step $\tilde{t}$.
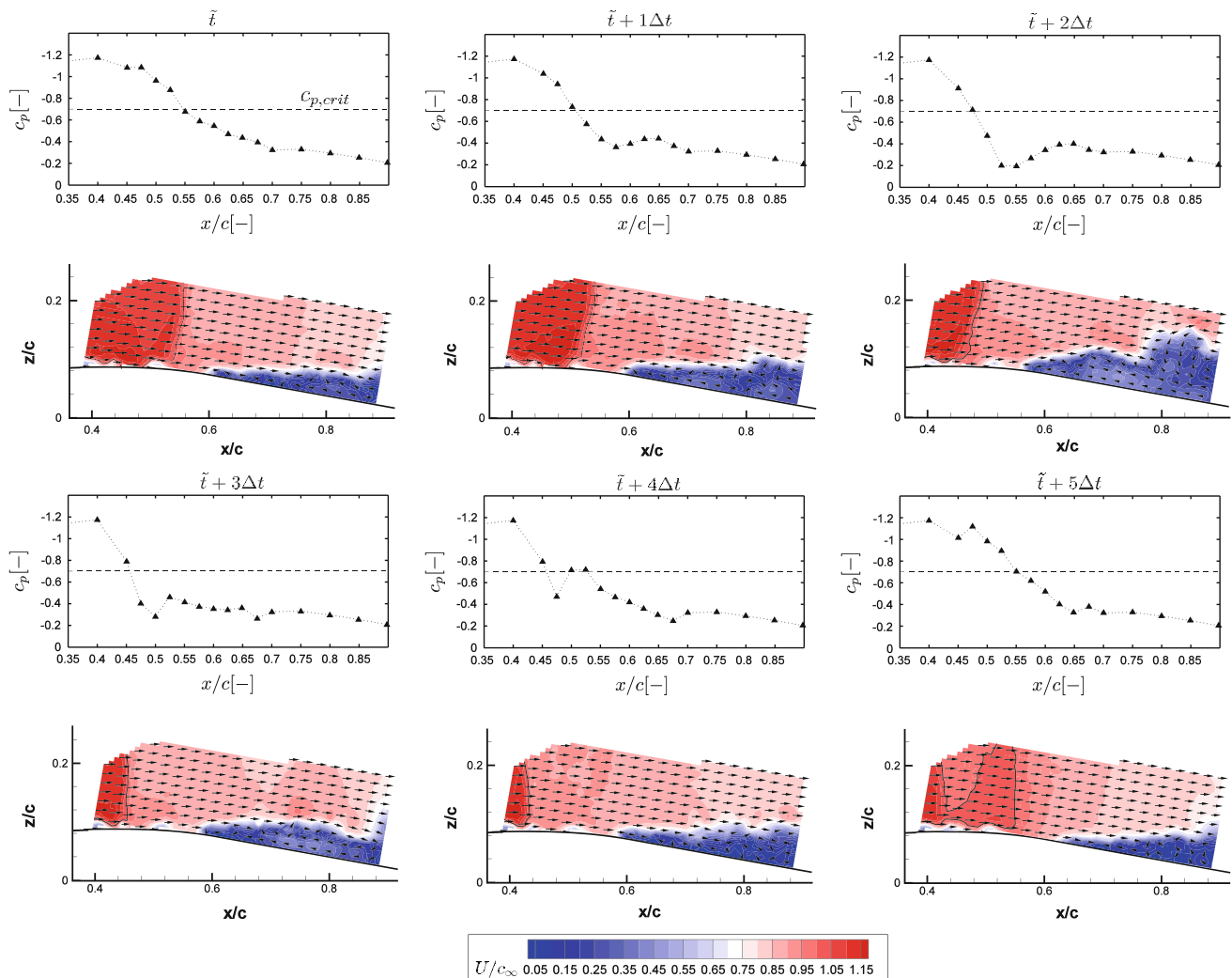
**Fig. 13** Time sequence of synchronously measured pressure distribution and velocity field at case II$_{as}$, time step $\Delta t = 0.67$ ms, the *black solid line* marks the $U/c_\infty = 1$ contour, every third vector plotted

At time steps $t = \tilde{t} + 3\Delta t$ and $\tilde{t} + 4\Delta t$, a rear separation of the boundary layer occurs far downstream of the shock wave. At the remaining time steps, the separation line is consistent with the location of the shock wave caused by the stronger pressure gradient across the shock. In the time steps $t = \tilde{t} + 3\Delta t$ and $\tilde{t} + 4\Delta t$, where the separation line is located downstream of the shock position, the shock wave is too weak to cause the boundary layer to detach. Note that the identification of the separation line is consistent with the data of the Schlieren images and can be done more precisely using the raw images of the TR-SPIV measurements.

An intermittent presence of the shock wave comparable to the flow behavior observed in the present study is described as Tijdeman type B shock motion. In this category, however, the shock wave disappears during part of its backward motion, while the disturbed DRA-2303 airfoil flow shows a disappearance of the shock close to the

upward end of its cycle. In Tijdeman type C motion, the shock also disappears during its upward motion, but with increasing shock strength and finally by propagating upstream as a sound wave into the incoming flow. The shock motion phenomenon of the disturbed DRA-2303 airfoil flow is quite different from the Tijdeman description, since the supersonic region decreases in strength to cause the weakening shock wave to disappear during its upward motion. Furthermore, the intensity of the disturbances generated in the freestream chamber is not changing with the shock position as it is the case for the noise produced at the trailing edge since the wall-bounded shear layer alters with the shock position. At the present case, this time invariant intensity of the sound waves coming from the freestream chamber and traveling upstream cause the shock wave to turn into an oblique shock at its most upstream position, and so the development of a second supersonic bubble is induced marking the beginning of a

new cycle. The formation of the oblique shock is likely to be connected with a decreasing shock strength at increasing position $z/c$ in the flow field. The weaker the shock, the stronger the impact of the upstream traveling sound waves is. Therefore, the sound waves force the shock further into the upstream direction at these positions further off the wall resulting in the shape of the observed oblique shock.

*3.2.2.3 Case $III_{as}$* The situation changes at case $III_{as}$, since the compressibility effects are more dominant. Therefore, in Fig. 14, the shock wave is present during the entire oscillation cycle, while the variation in strength of the supersonic field is generally smaller. Note that compared to the flow field at case $II_{as}$, the velocity field at $M_\infty = 0.76$ shows a significant difference in the flow behavior regarding the trailing-edge separation. In the former case, the separation originates closer to the trailing edge and extends upstream to the instantaneous shock-foot line when the shock wave is located close enough to the trailing edge, e.g., at time steps $t = \tilde{t}$, $\tilde{t} + 1\Delta t$, and $\tilde{t} + 5\Delta t$ in Fig. 13. In the latter case $III_{as}$, the mean strength of the shock wave is generally higher, thus inducing the separation during the entire oscillation cycle. This agreement between the shock-foot location and the separation line is accompanied by a reduction in the amplitude of the oscillation. Furthermore, the sound pressure level of the tunnel disturbances compared to the intensity of the sound waves generated at the trailing edge has decreased significantly since the source in the freestream chamber is relatively further away at increasing freestream velocities with the sound waves propagating upstream with $c - u_\infty$. This becomes obvious by the change of the shock motion from a Tijdeman type B–A. The shock itself is generally stronger such that it is less sensitive to any kind of
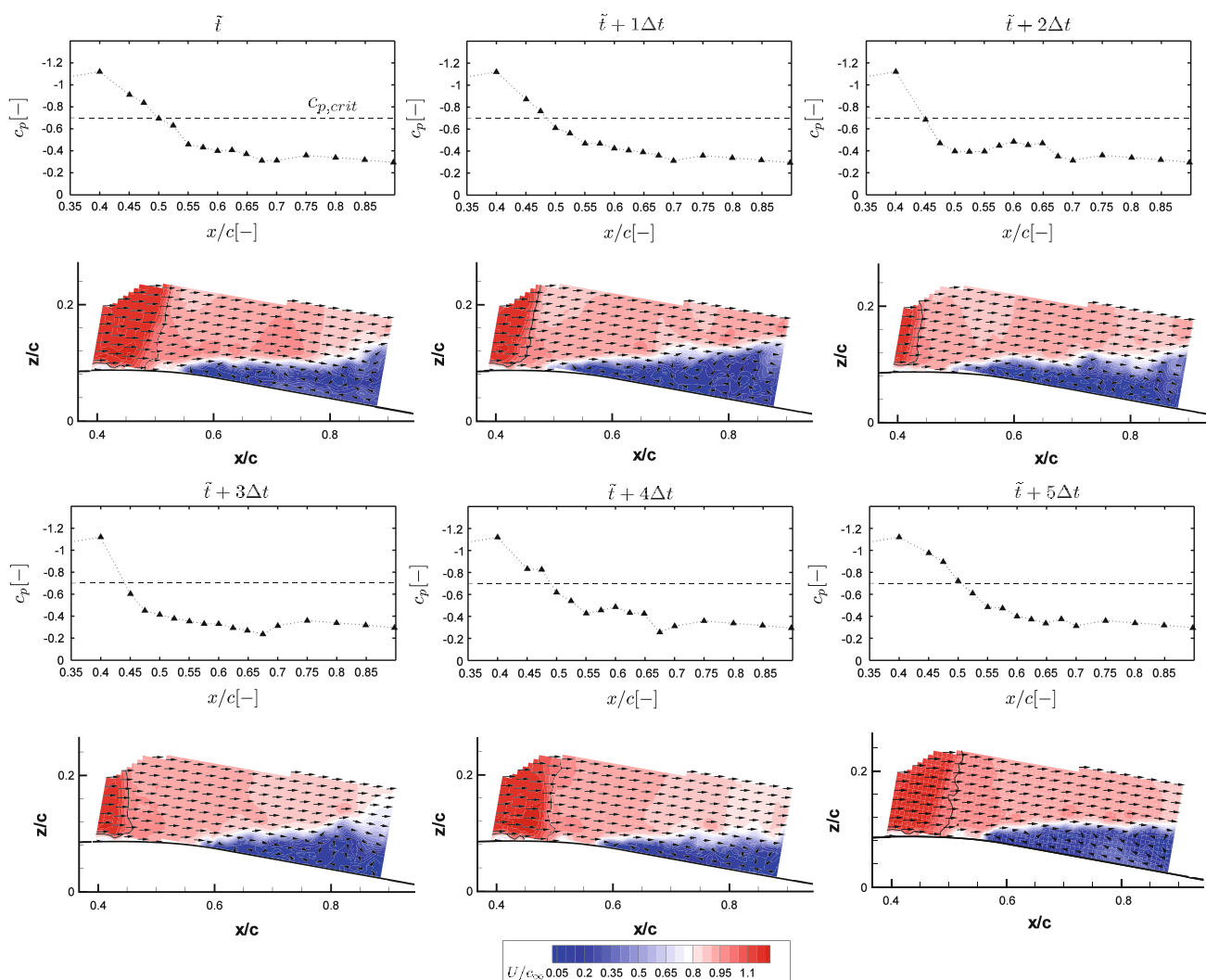


**Fig. 14** Time sequence of synchronously measured pressure distribution and velocity field at case $III_{as}$, time step $\Delta t = 0.67$ ms, the *black solid line* marks the $U/c_\infty = 1$ contour, every third vector plotted

disturbance which causes its displacement into the upstream direction. At the beginning of the cycle, at time step $t = \tilde{t}$, the source at the trailing edge and the tunnel resonance act together and cause the shock wave to travel upstream in the subsequent time steps. This mechanism holds until time step $\tilde{t} + 2\Delta t$ where the extension of the separation at the trailing edge has increased compared to time step $\tilde{t}$ such that the sound pressure level of the noise generated at the trailing edge has decreased as described above for the non-disturbed flow. At time steps $\tilde{t} + 3\Delta t$ to $\tilde{t} + 5\Delta t$, the shock wave moves downstream until it reaches its most downstream position and the cycle starts again with the less extended separation of the boundary layer causing an increased sound pressure level of the trailing-edge noise at the shock position. The accordance of the position of the shock foot and the extension of the separation has also reduced the unsteady behavior of the flow which is why the amplitude of the shock oscillation is decreased from 13% chord to 6% chord at case III$_{as}$. The existence of a steady flow case at higher Mach numbers is also described by Xiao and Tsai (2006) on a circular arc airfoil at a thickness of 18% and by Geissler (2003) for the NLR 7301 airfoil in the context of numerically simulated limit-cycle oscillations.

## 4 Conclusion

Results from an experimental investigation of transonic flows around a DRA-2303 supercritical airfoil have been presented. The airfoil aerodynamics has been investigated for angles of attack ranging from $\alpha = 0$–$4°$, freestream Mach numbers between $M_\infty = 0.64$ and $0.78$, and Reynolds numbers $Re_\infty$ related to the chord length $c$ on the order of $10^6$. Three transonic flows are discussed in detail. These flows have been investigated on the one hand, with the wind tunnel in standard configuration, and on the other hand, without the freestream chamber walls generating an acoustic source downstream of the test section. Time-resolved stereo particle-image velocimetry was used to display the dynamic interaction between the oscillating shock wave and the separated flow in the rear part of the airfoil.

Three buffet flows case II$_{as}$, and case III$_{as}$, and case II at $[\alpha_{as}, M_{\infty,as}] = [3°, 0.72]$, $[\alpha_{as}, M_{\infty,as}] = [3°, 0.76]$, and $[\alpha, M_\infty] = [3°, 0.72]$, respectively, with a dynamic shock–boundary layer interaction have been identified. The first two buffet flows have been influenced by an acoustic source downstream of the test section with upstream-propagating sound waves comparable to the trailing-edge noise considered as the main feature for the buffet phenomenon (Lee 2001). Thereby, the frequency of the generated noise excited the second mode of the natural buffet

frequency of the airfoil such that both sources—the trailing-edge noise and the noise generated in the freestream chamber—are linked. The latter, non-disturbed flow, exhibits an oscillatory shock motion only due to the local feedback loop formed by the shock wave and the trailing-edge noise of the airfoil.

The $M_{\infty,as} = 0.72$ flow at case II$_{as}$ exhibits a highly dynamic local interaction of a weak shock with a marginal trailing-edge separation, and the $M_{\infty,as} = 0.76$ flow at case III$_{as}$ is dominated by a stronger shock wave associated with a severe but less dynamic trailing-edge separation. At the $M_{\infty,as} = 0.72$ flow, the noise generated in the freestream chamber dominates the interaction and the varying intensity of the trailing-edge noise is negligible. The results demonstrate a significant reduction in the unsteadiness of the second flow case at higher Mach number $M_{\infty,as} = 0.76$, where the intensity of the noise generated in the freestream chamber is generally smaller at the test section, and the trailing-edge noise becomes a major part for the noise production and thus the shock motion. The accordance of the position of the shock foot and the extension of the boundary-layer separation has been identified to be responsible for this reduction of the unsteadiness since the latter directly influences the sound pressure level of the trailing-edge noise at the shock position. Furthermore, for the non-disturbed buffet flow at $M_\infty = 0.72$, case II, solely the alternating sound pressure level of the trailing-edge noise could be identified to be responsible for the shock movement. This conclusion results from the comparison of the behavior of the interaction of the disturbed and the non-disturbed flows. The shock wave displacement into the upstream direction is associated with upstream-propagating disturbances generated at the trailing edge. This mechanism holds until the sound pressure level at the location of the shock wave becomes too weak at increasing extension of the separation and the shock wave travels back to its origin location marking the beginning of a new cycle. Finally, the pulsation of the separation could be determined to be a reaction to the shock motion and not vice versa.

## References

Adamson TC Jr, Messiter AF (1980) Analysis of two-dimensional interactions between shock waves and boundary layers. Ann Rev Fluid Mech 12:103–138

Amecke J (1985) Direkte Berechnung von Wandinterferenzen und Wandadaption bei zweidimensionaler Strömung in Windkanälen mit geschlossenen Wänden. DFVLR-FB, pp 85–62

Binion TW (1988) Potentials for pseudo-reynolds number effects. In: Reynolds number effects in transonic flow. AGARDograph vol 303, sect. 4

Brunet V, Deck S, Jacquin L, Molton P (2006) Transonic buffet investigations using experimental and des techniques. In: Proceedings of the 7th ONERA-DLR aerospace symposium ODAS 2006, Toulouse, France. ONERA-TP-2006-165

Deck S (2005) Numerical simulation of transonic buffet over a supercritical airfoil. AIAA J 43(7):1556–1566

Délery JM (1985) Shock wave/turbulent boundary layer interaction and its control. Progr Aerosp Sci 22:209–280

Délery J, Marvin JG (1986) Shock-wave boundary layer interactions. AGARDograph 280:90–108

Elsinga GE, van Oudheusden BW, Scarano F (2005) Evaluation of aero-optical distortion effects in PIV. Exp Fluids 39:246–256. doi:10.1007/s00348-005-1002-8

Finke K (1977) Stoßschwingungen in schallnahen Strömungen. VDI-Forschungsheft, vol 580. Verlag, Düsseldorf

Geissler W (2003) Numerical study of buffet and transonic flutter on the NLR 7301 airfoil. Aerosp Sci Technol 7:540–550

Green JE (1970) Interactions between shock waves and turbulent boundary layers. Progr Aerosp Sci 11:235–340

Guntermann P (1992) Entwicklung eines Profilmodells mit variabler Geometrie zur Untersuchung des Transitions-verhaltens in kompressibler Unterschallströmung. Verlag, ISBN: 3-86111-365-1

Hartmann A, Steimle PC, Klaas M, Schröder W (2011) Time-resolved particle-image velocimetry of unsteady shock wave-boundary layer interaction. AIAA J 49(1):195–204. doi:10.2514/1.J050635

Lee BHK (2001) Self-sustained shock oscillations on airfoils at transonic speeds. Progr Aerosp Sci 37:147–196

Lee BHK, Murty H, Jiang H (1994) Role of kutta waves on oscillatory shock motion on an airfoil. AIAA J 32(4):789–796

Melling A (1986) Seeding gas flows for laser anemometry. In: Proceedings on the conference of advanced instrumentation for aero engine components. AGARD CP-399, p 8.1

Pearcey HH, Osborne J, Haines AB (1968) The interaction between local effects at the shock and rear separation: a source of significant scale effects in wind-tunnel tests on aerofoils and wings. Transonic aerodynamics. AGARD-CP-35, pp 11.1–11.23

Raffel M, Willert CE, Wereley ST, Kompenhans J (2007) Particle image velocimetry: a practical guide. Springer, Berlin

Raveh DE, Dowell EH (2009) Frequency lock-in phenomenon in oscillating airfoils in buffeting transonic flows. International forum on aeroelasticity and structural dynamics. IFASD-2009-135

Romberg H-J (1990) Two-dimensional wall adaption in the transonic wind tunnel of the AIA. J Aircr 38(4):177–180

Schewe G, Knipfer A, Mai H, Dietz G (2002) Experimental and numerical investigation of nonlinear effects in transonic flutter. German aerospace centre internal report DLR-IB 232-2002J 01

Seddon J (1960) The flow produced by interaction of a turbulent boundary layer with a normal shock wave of strength sufficient to cause separation. RAE TM Aero 667, R&M 3502

Stanewsky E, Delery J, Fulker J, de Matteis P (1997) Drag reduction by shock and boundary layer control. Results of the project EUROSHOCK, AER2-CT92-0049. Notes on numerical fluid mechanics, vol 56. Springer, Berlin

Tijdeman H (1965) Theoretical and experimental results for the dynamic response of pressure measuring systems. NLR-TR F.238

Tijdeman H (1977) Investigation on the transonic flow around oscillating airfoils. PhD thesis, NLR TR 77090 U, TU Delft, The Netherlands

Tropea C, Foss J, Yarin A (2007) Handbook of experimental fluid mechanics. Springer, Berlin

Tsai RY (1986) An efficient and accurate camera calibration technique for 3-D machine vision. In: Proceedings of IEEE conference on computer vision and pattern recognition, pp 364–374

Westerweel J, Scarano F (2005) Universal outlier detection for PIV data. Exp Fluids 39:1096–1100. doi:10.1007/s00348-005-0016-6

Willert C (1997) Stereoscopic particle image velocimetry for application in wind tunnel flows. Meas Sci Technol 8:1465–1479

Xiao Q, Tsai HM (2006) Numerical study of transonic buffet on a supercritical airfoil. AIAA J 44(3):620–628